BoCXS Project: updates on the conceptual design and feasibility study

Giovanni Campri

Elettra Sincrotrone Trieste

INFN LNF
Istituto Nazionale di Fisica Nucleare

Bologna Compton X-ray Source

Massimo Placidi, Guest Lawrence Berkeley National Laboratory;
massimoplacidi@icloud.com

Giovanni Campri, Sapienza University of Rome;
giovanni.campri@uniroma1.it

Anna Giribono, **David Alesini**, INFN-LNF;
Anna.Giribono@lnf.infn.it (A.G.); david.alesini@lnf.infn.it (D.A.)

Simone Di Mitri, Elettra-Sincrotrone Trieste;
simone.dimitri@elettra.eu

Armando Bazzani, **Giorgio Turchetti**, University of Bologna;
armando.bazzani@unibo.it (A.B.); giorgio.turchetti@unibo.it (G.T.)

This project has received funding from the European Union’s Horizon 2020 Research and Innovation programme under GA No101004730

The BoCXS proposal

Bologna Compton X-ray Source → ICS-based light source

Massimo Placidi, Guest Lawrence Berkeley National Laboratory;
massimoplacidi@icloud.com

Giovanni Campri, Sapienza University of Rome;
giovanni.campri@uniroma1.it

Anna Giribono, **David Alesini**, INFN-LNF;
Anna.Giribono@lnf.infn.it (A.G.); david.alesini@lnf.infn.it (D.A.)

Simone Di Mitri, Elettra-Sincrotrone Trieste;
simone.dimitri@elettra.eu

Armando Bazzani, **Giorgio Turchetti**, University of Bologna;
armando.bazzani@unibo.it (A.B.); giorgio.turchetti@unibo.it (G.T.)

High quality X-ray beam

- Tunable energy (50-700 keV)
- Quasi-monochromatic
- Short pulses (ps)
- Reasonably high fluxes ($\sim 10^{10}$ ph/s)

Multidisciplinary applications

- Biomedical imaging
- Industrial applications
- Cultural heritage science
- …and more!

This project has received funding from the European Union's Horizon 2020 Research and Innovation programme under GA No101004730

BoCXS beam dynamics study

High quality X-ray beam ⟷ High quality e-beam

We performed an electron beam dynamics simulation from the photocatode to the IP, in order to obtain a realistic set of parameters to characterise the Compton X-rays.

The photo-injector, where the space-charge effects are dominant, was simulated using ASTRA. The beam transport and focusing to the IP was simulated in elegant (CSR included).

This study was crucial to shape the final design of the machine.

https://www.desy.de/~mpyflo/
https://www.aps.anl.gov/Accelerator-Operations-Physics/Software#elegant

BoCXS original design

Bologna Compact X-ray Source

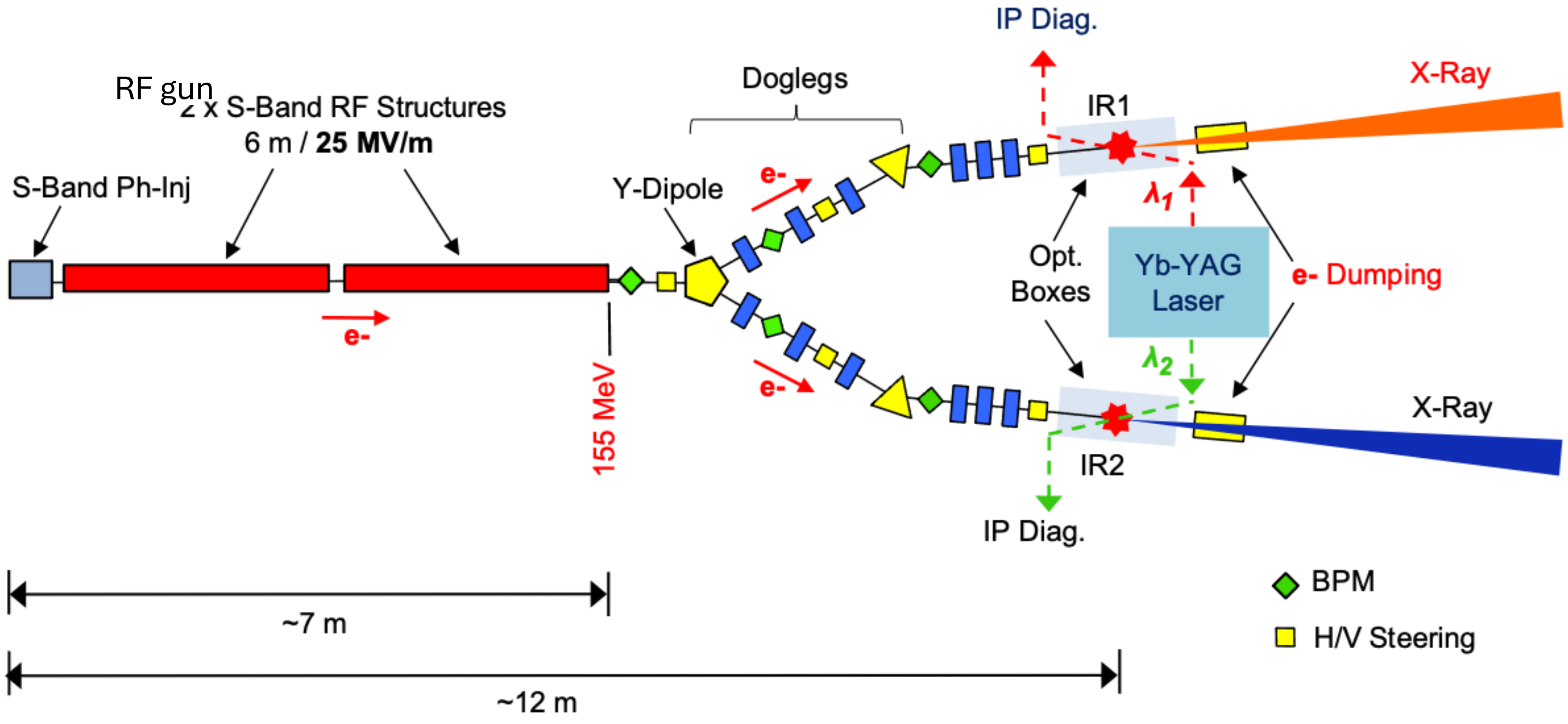

Fig. 1 – Original full S-Band configuration of the BoCXS X-ray source. Electron bunches accelerated up to 155 MeV in an S-Band Linac are transported up to the interaction regions IR1 and IR2 where they interact with photon pulses produced by a laser system operating on the fundamental wavelength ($\lambda_{ph}^0 = 1032\, nm$) or its 2nd harmonic. ICS X-ray pulses are emitted in two different energy ranges alternatively feeding two user areas.

BoCXS updated layout

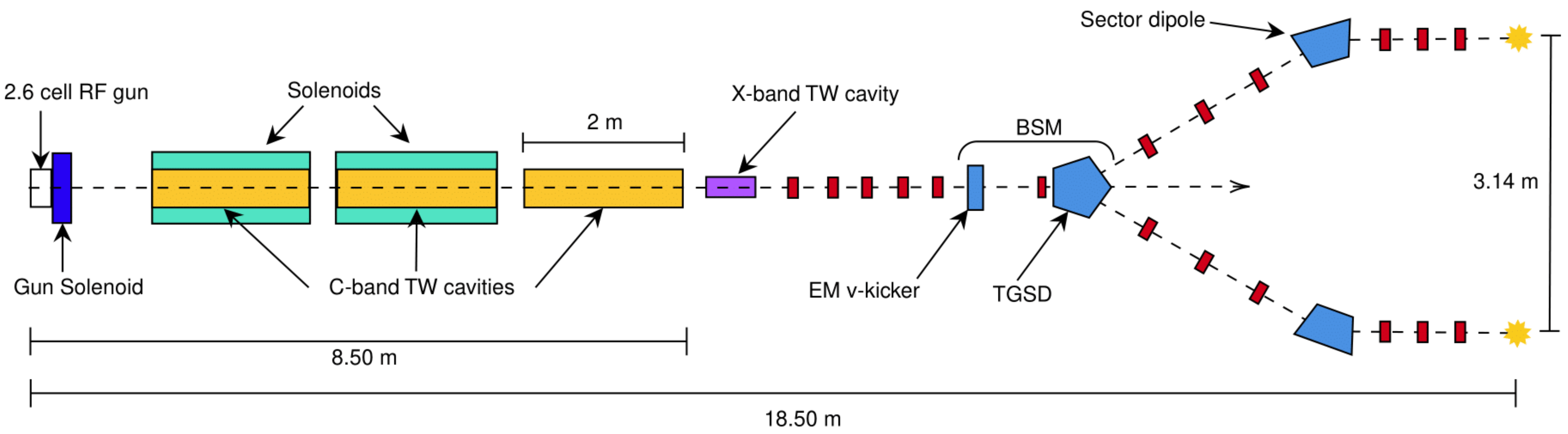

Fig. 2 – BoCXS schematic machine layout (not to scale). These are all the elements included in the beam simulations.

Main upgrades

Fully redesigned C-band photo-injector
X-band linearizer
Matching section
BSM in place of the Y-dipole
A third line for e-beam applications

Bologna Compact X-ray Source

BoCXS updated layout

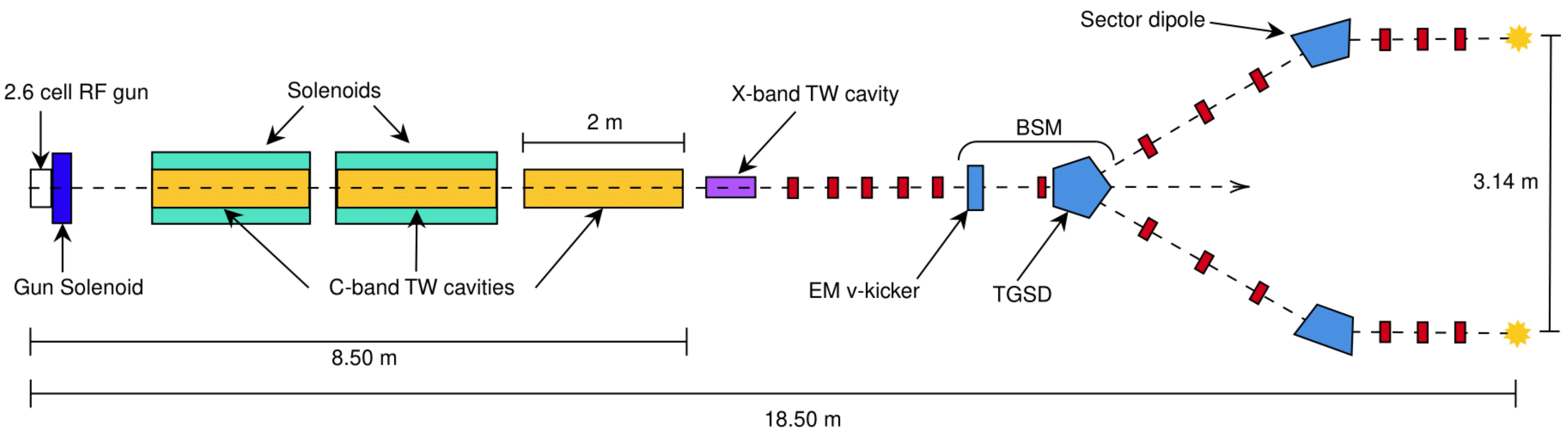

Fig. 2 – BoCXS schematic machine layout (not to scale). These are all the elements included in the beam simulations.

Main upgrades

Fully redesigned C-band photo-injector
X-band linearizer
Matching section
BSM in place of the Y-dipole
A third line for e-beam applications

Bologna ~~Compact~~ X-ray Source
Compton

C-band photo-injector

Normal conductive structure

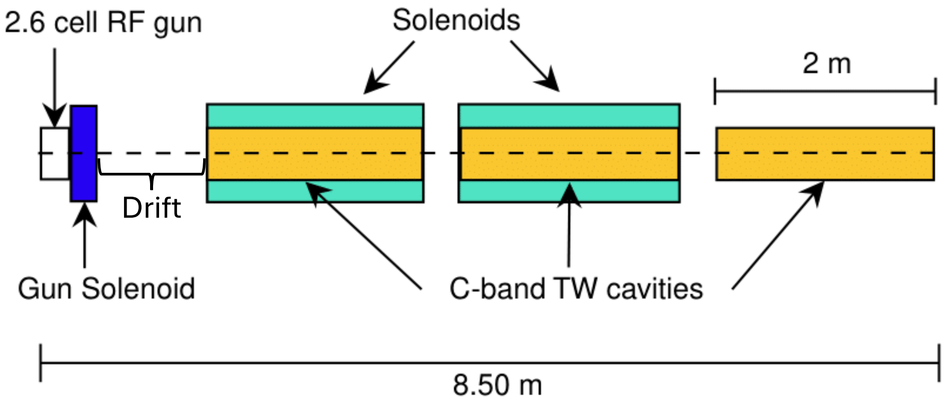

Fig. 3 – Photo-injector layout.

Tab. 1 – Photo-injector parameters

Parameter	Value
C-band resonant frequency [GHz]	5.712
Rep. rate [kHz]	0.1
Gun peak field [MV/m]	180
TW Cavities peak field [Mv/m]	40

The redesign of the photo-injector and the addition of a matching section after the linac led to an even larger footprint.

A C-band accelerating structure allows to sustain higher gradients at normal conducting temperatures while decreasing the breakdown rate probability, thus reducing the space needed for acceleration.

A higher peak field also enhances machine performance in terms of beam brightness.

INFN LNF

A. Giribono, et al., **Dynamics studies of high brightness electron beams in a normal conducting, high repetition rate C-band injector**, Phys. Rev. Accel. Beams 26, (2023).

C-band photo-injector optimisation

Simulated with ASTRA (500k particles)

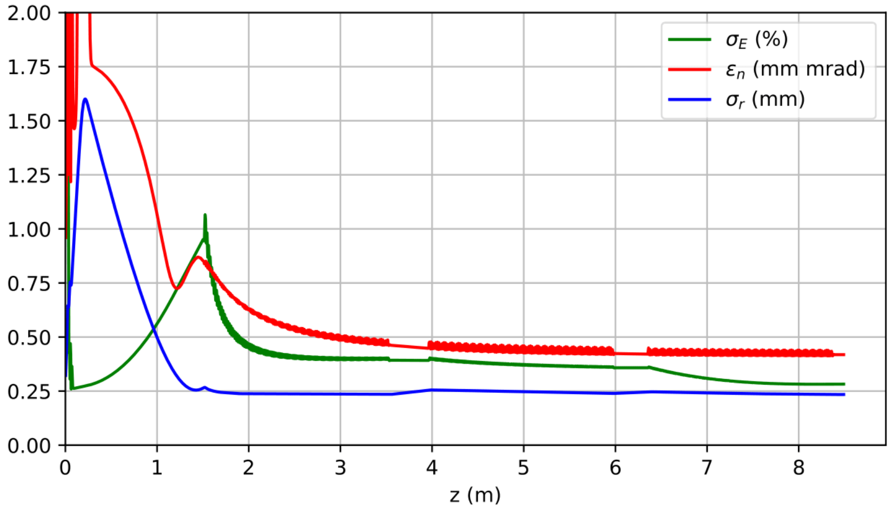

Fig. 4 – Simulation of beam evolution along the C-band photo-injector.

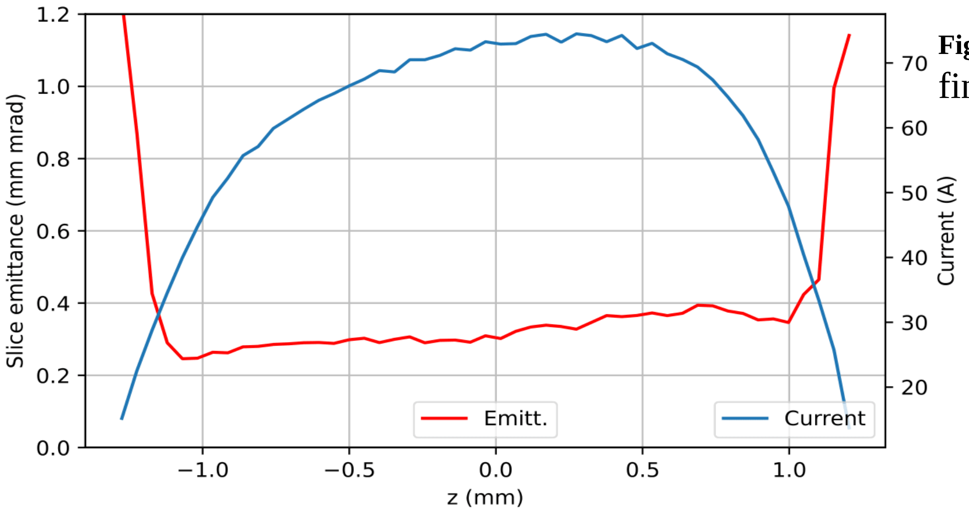

Fig. 5 – Slice analysis of the final beam.

Tab. 2 – Optimised working point parameters for the C-band photo-injector (on-crest operation)

Photocathode laser

Parameter	Value
Laser rms spot size (Uniform) [mm]	0.3
FWHM length pulse (Flat top) [ps]	8.5
Rise time [ps]	0.5
Beam energy [MeV]	190.3
Bunch charge [nC]	0.5
Norm. proj. emittance [mm mrad]	0.42
Bunch length, rms [ps]	2.1
Transverse beam size, rms [mm]	0.23
Relative energy spread, rms [%]	0.28
Peak current [A]	75

Linearization with the X-band cavity

The need for linearization

The chromatic aberrations in the quadrupoles had a large impact on the beam emittance.

A significant current profile modulation inside the doglegs, due to the coupling of R_{56} with the energy chirp, caused beam quality degradation through Coherent Synchrotron Radiation (CSR) effects.

The cause was a strong quadratic energy chirp, due to the curvature of the RF fields inside the C-band photo-injector.

All these effects caused emittance growth of up to 100%, and made it very difficult to optimise the magnetic lattice.

Linearization with the X-band cavity

The need for linearization

The chromatic aberrations in the quadrupoles had a large impact on the beam emittance.

A significant current profile modulation inside the doglegs, due to the coupling of R_{56} with the energy chirp, caused beam quality degradation through Coherent Synchrotron Radiation (CSR) effects.

The cause was a strong quadratic energy chirp, due to the curvature of the RF fields inside the C-band photo-injector.

All these effects caused emittance growth of up to 100%, and made it very difficult to optimise the magnetic lattice.

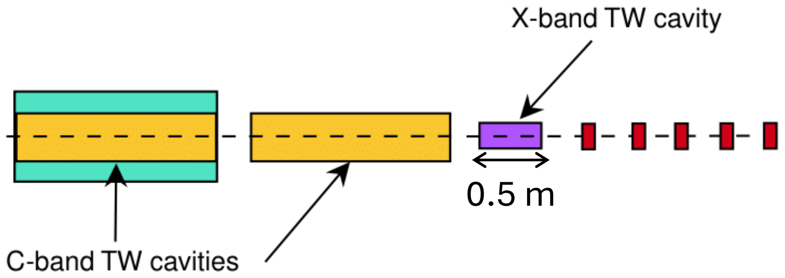

Fig. 6 – Portion of the beamline containing the X-band linearizer.

Energy gain in the C-band cavities:

$$E_C \approx e\Delta V_C \cos\phi_C - e\Delta V_C k_C z \sin\phi_C - \frac{e\Delta V_C}{2} k_C^2 z^2 \cos\phi_C + o(z^3)$$

$(\phi_C = 0)$ On-crest operation

Final energy:

$$E_f \approx E_C + e\Delta V_X \cos\phi_X - e\Delta V_X k_X z \sin\phi_X - \frac{e\Delta V_X}{2} k_X^2 z^2 \cos\phi_X + o(z^3)$$

$(\phi_X = \pi)$ The linearizer decelerates the beam

$$\Delta V_X = \frac{k_C^2}{k_X^2} \Delta V_C$$

Effects of the linearization

Simulated with elegant (500k particles)

Fig.7 – Beam longitudinal phase space.

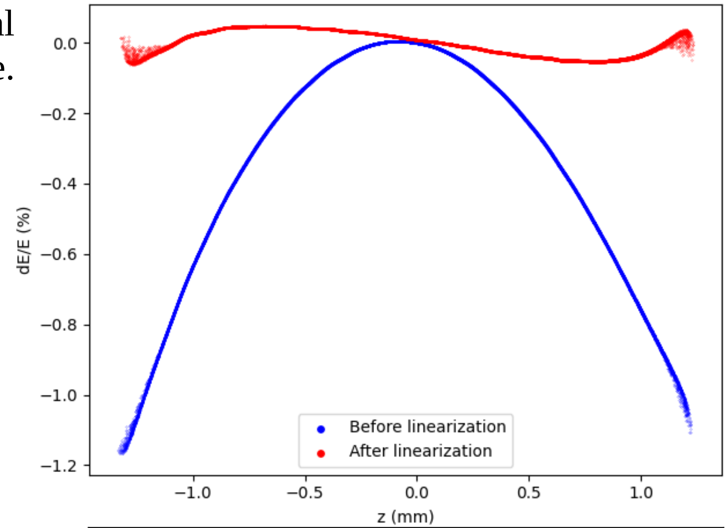

Fig. 8 – Beam current.

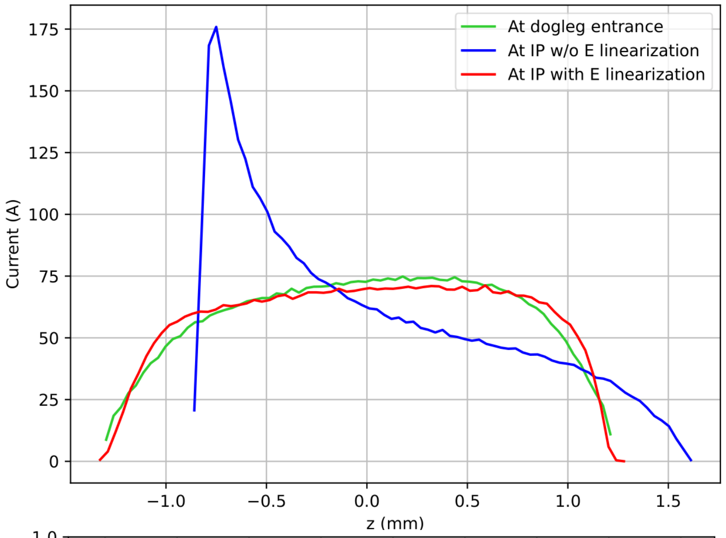

Fig. 9 – Relative energy distribution.

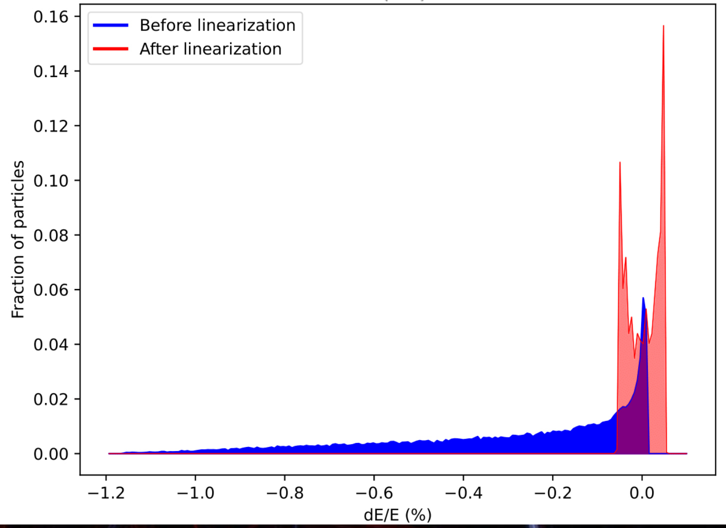

Fig. 10 – Horizontal achromatic emittance evolution.

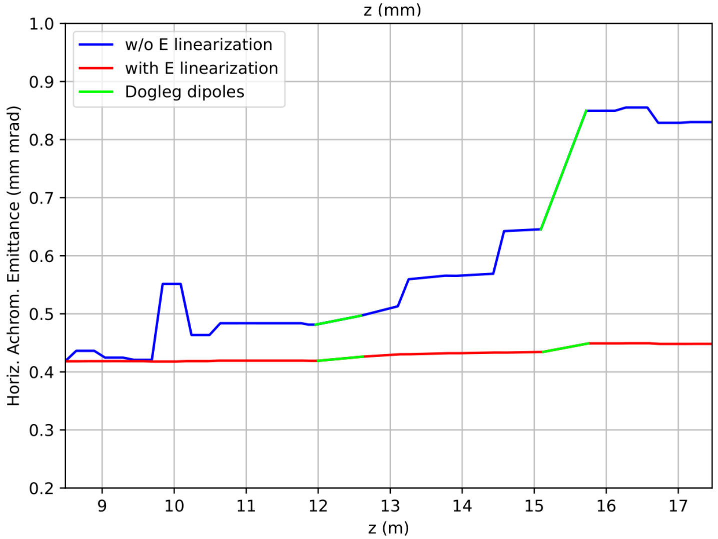

Effects of the linearization

Tab. 3 – X-band cavity parameters

Parameter	Value
X-band resonant frequency [GHz]	11.424
Rep. rate [kHz]	0.1
X-band cavity field [MV/m]	92.4
Injection phase [deg]	179.72
X-band cavity length [m]	0.5
Beam final relative energy spread, rms [%]	0.03
Beam final energy [MeV]	145

$$B = \frac{Q}{\varepsilon_{nx}\varepsilon_{ny}\sigma_t\sigma_E} \approx 10^{18}\ [\mathrm{A/m^2}]$$

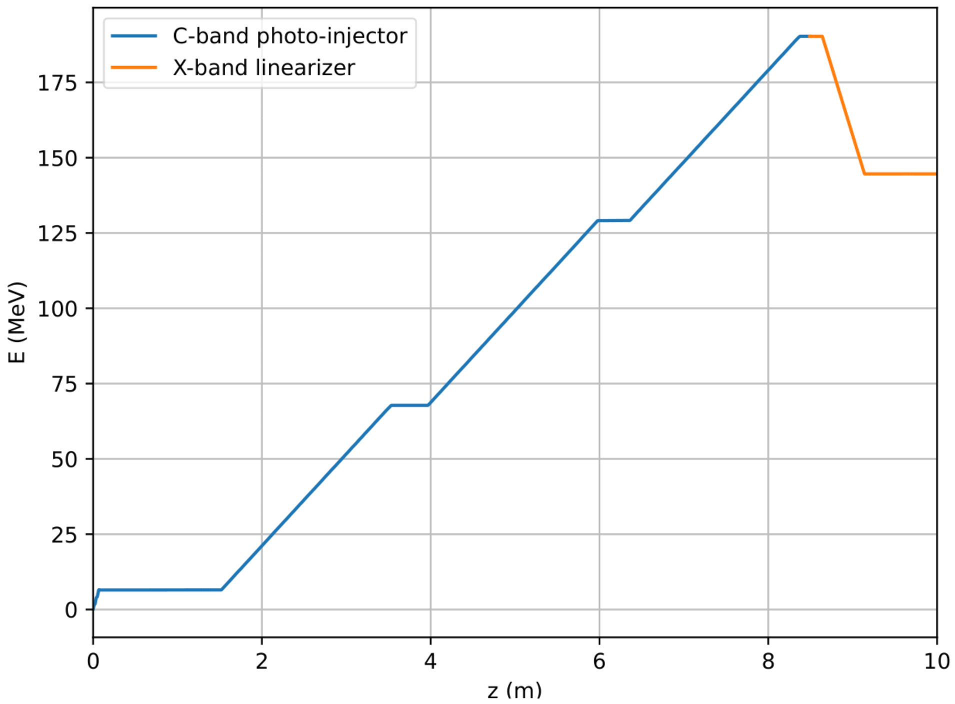

Fig. 11 – Beam energy evolution along the RF structures. The decelerating effect of the X-band cavity brings the final energy to 145 MeV.

Bunch Selection Module (BSM)

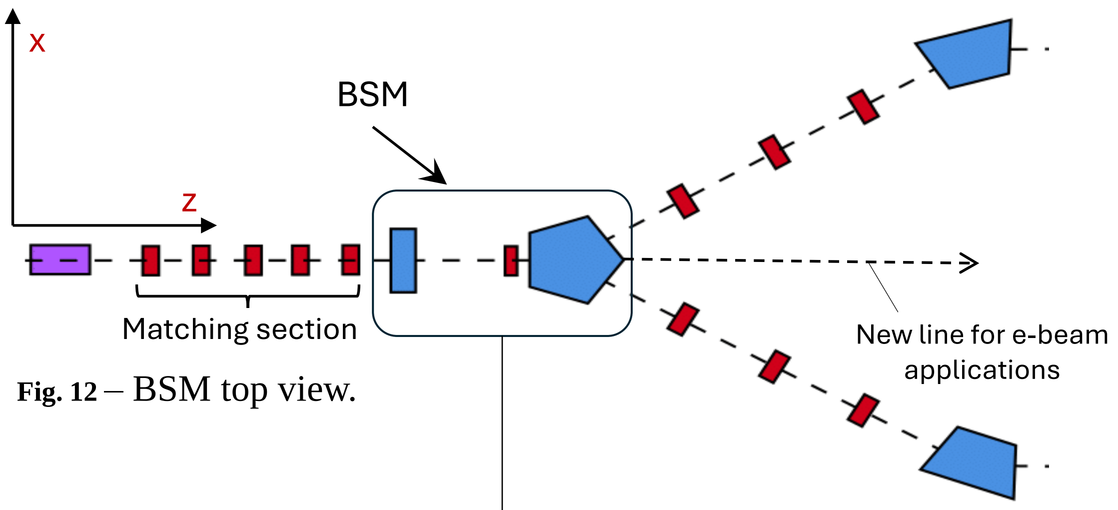

Fig. 12 – BSM top view.

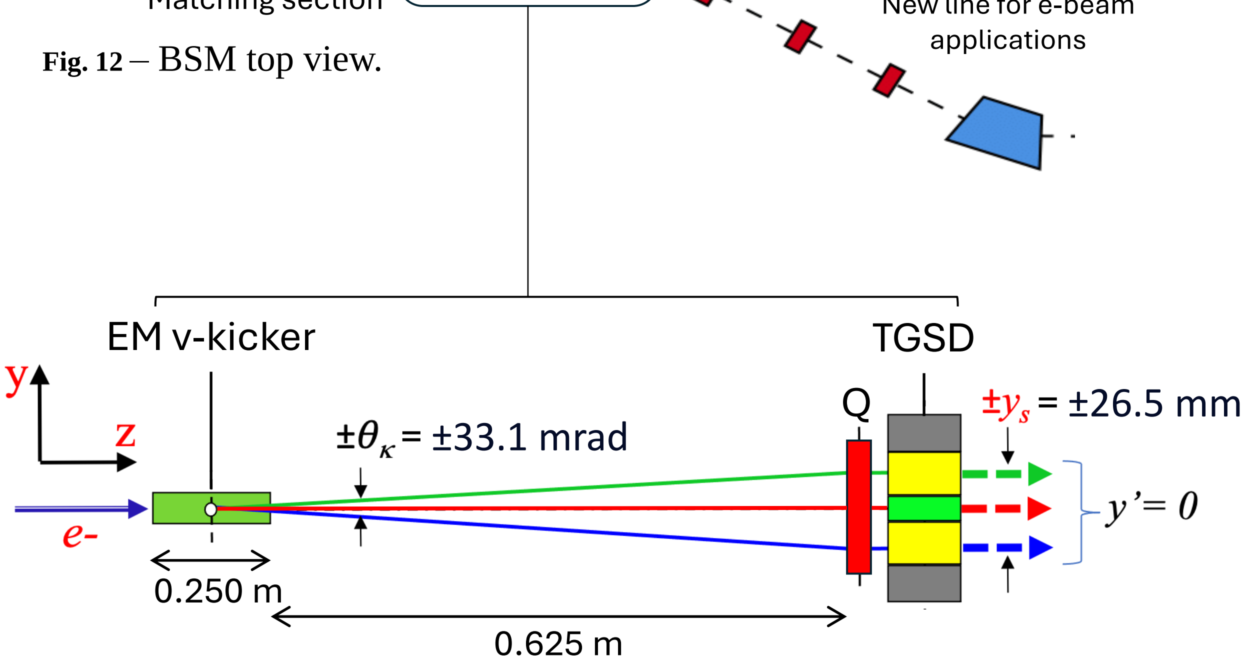

Fig. 13 – BSM side view.

Bunch Selection Module (BSM)

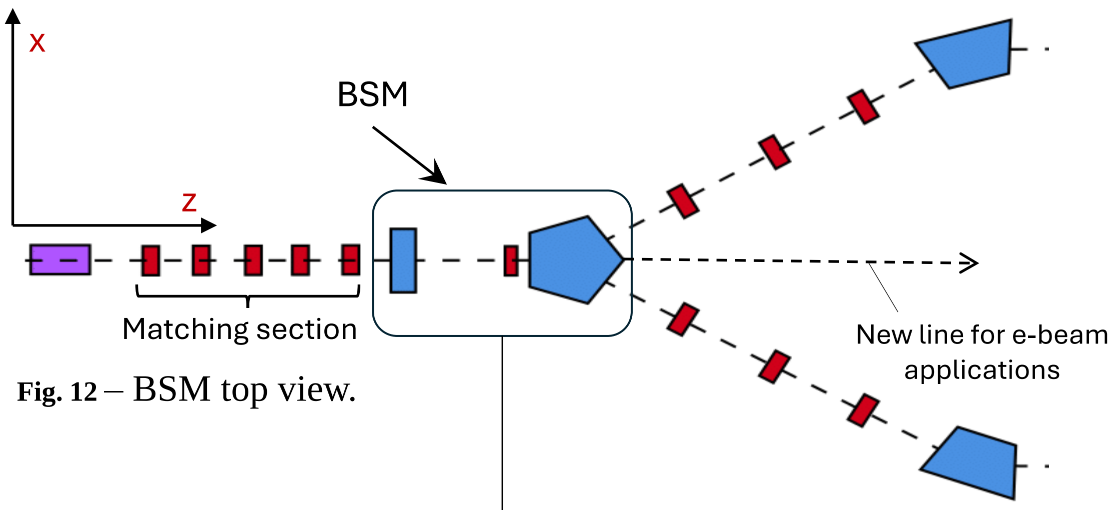

Fig. 12 – BSM top view.

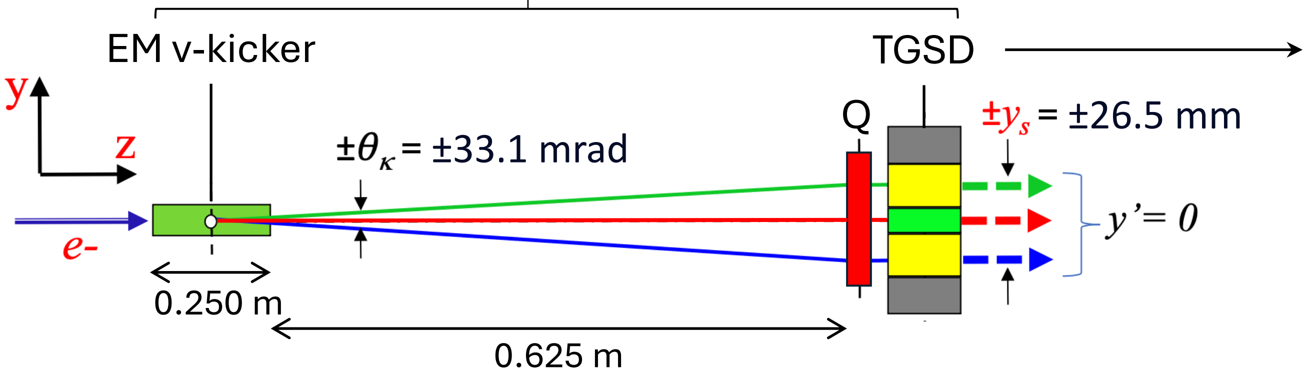

Fig. 13 – BSM side view.

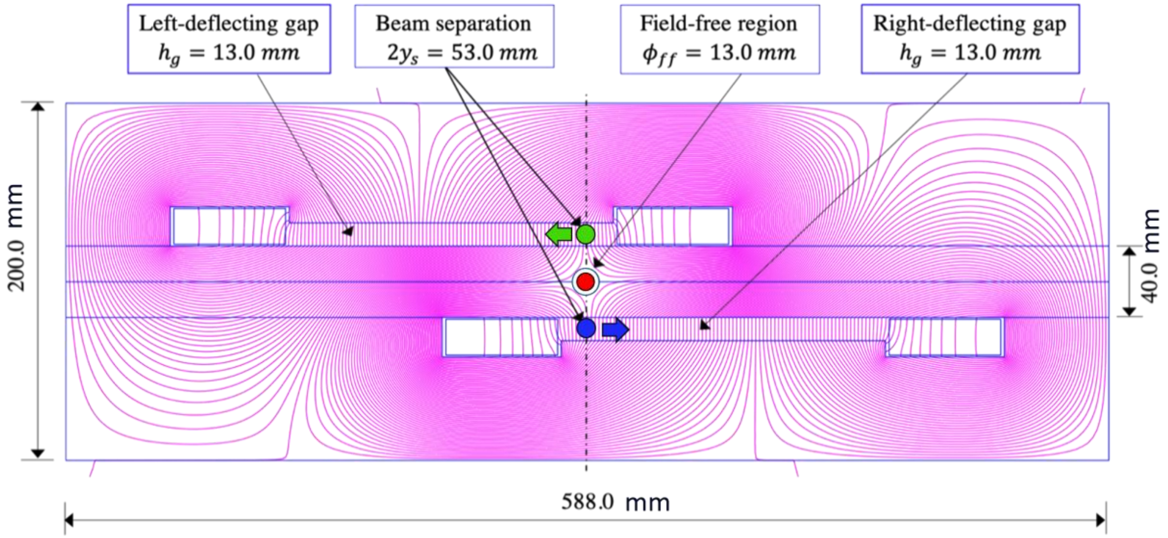

Fig. 14 – Front view vertical section of the Poisson-optimized Twin-Gap Septum Dipole (TGSD).

Bunch Selection Module (BSM)

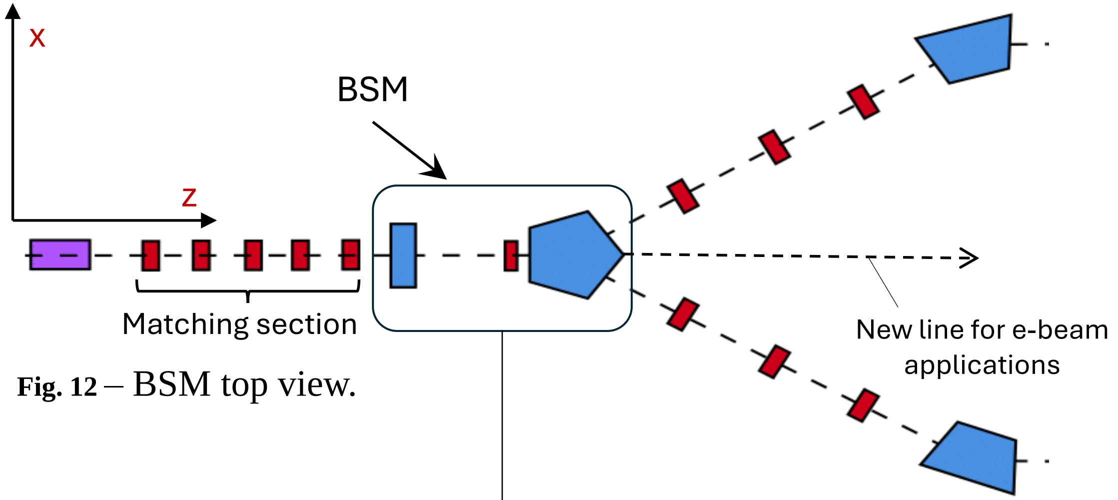

Fig. 12 – BSM top view.

Multimode operation

BSM scheme provides the possibility to select the beamline on a bunch-by-bunch basis, allowing a quasi-simultaneous operation of up to three user areas.

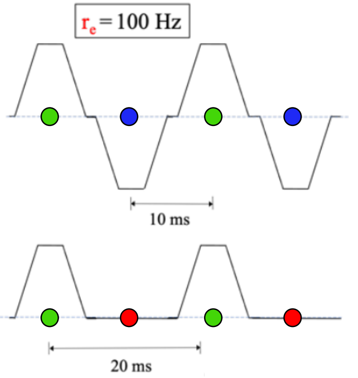

Fig. 15 – Examples of possible deflecting patterns.

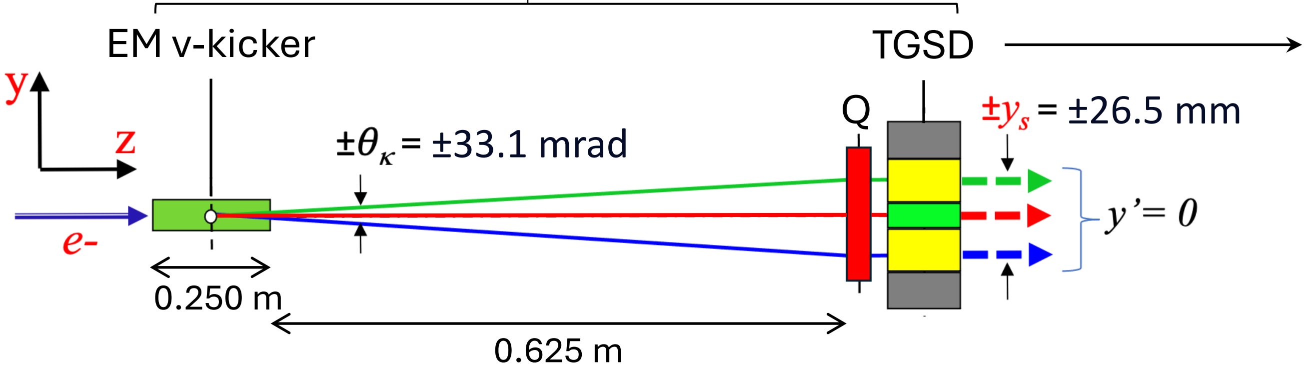

Fig. 13 – BSM side view.

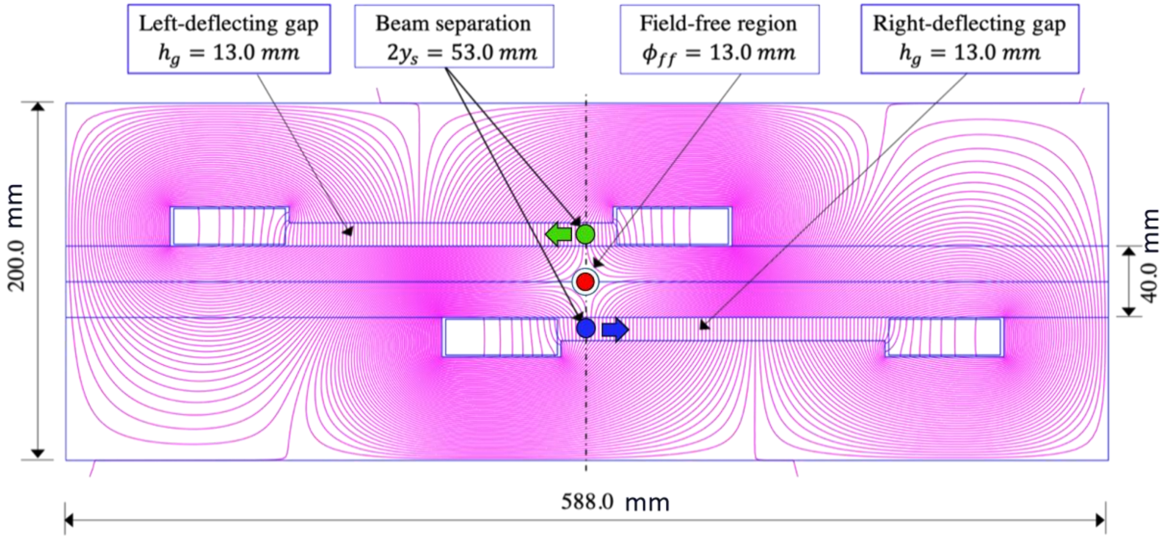

Fig. 14 – Front view vertical section of the Poisson-optimized Twin-Gap Septum Dipole (TGSD).

BSM and e-beam application

Tab. 4 – BSM parameters

Parameter	Value
V-kicker	
Rep. rate [kHz]	0.1
Rise time [μs]	~5
Pulse duration [μs]	50
Deflecting field [T]	±0.064
Quadrupole	
Strength [m^ − 2]	-12.78
Core length [mm]	100.0
TGSD	
Nominal deflection [deg]	±30
Arc length [mm]	628.0
B-field [T]	±0.403

Tab. 5 – Parameters for a dedicated FLASH-RT application. The doses are normalized to a 10 g sample

Parameter	Value
Bunch charge [nC]	0.5
Pulse width (FWHM) [ps]	7.2
Electron energy [MeV]	190
Rep. rate [kHz]	0.1
Bunch energy [mJ]	95.0
Pulse current [A]	69.3
Average current [nA]	50.0
Pulse dose [Gy]	9.5
Pulse dose rate [Gy/s]	$1.3 \cdot 10^{12}$
Average dose rate [Gy/s]	950

These are maximum values. Multimode operation would result in a fraction of this performance.

Beam transport and focusing to the IP

Fig. 16 – Beam transport line to the IP.

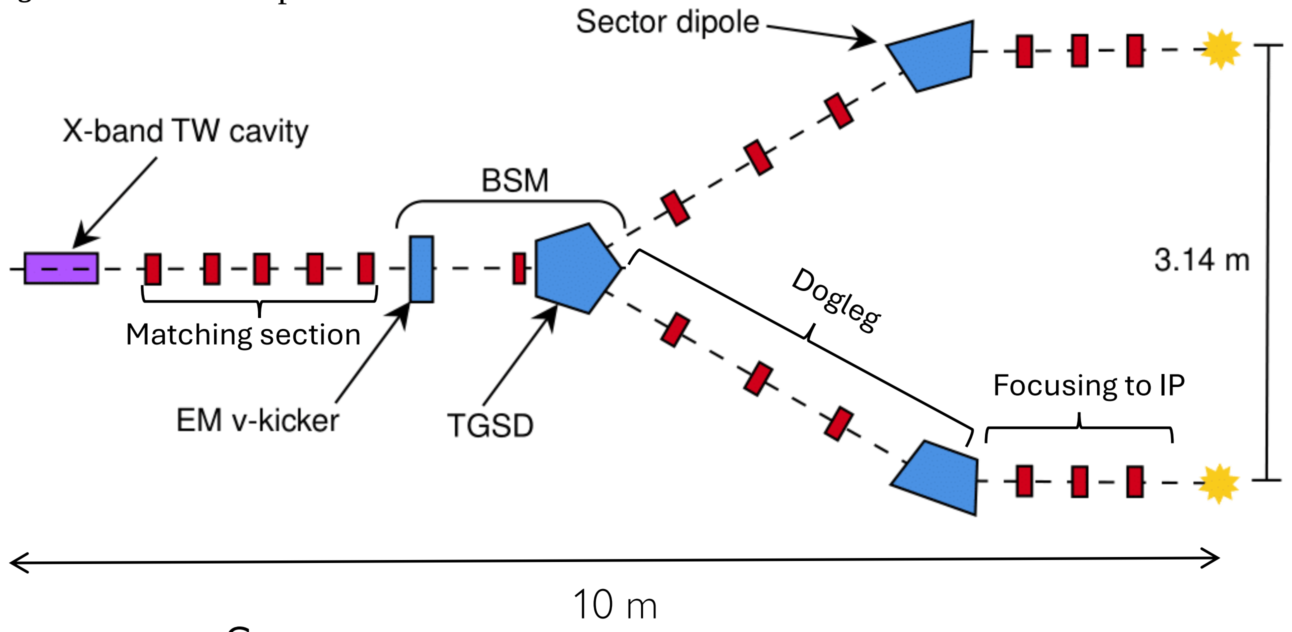

Simulated with elegant (500k particles)

We performed a full optimisation of the magnetic lattice using elegant (no space charge).

The the beam dynamics is mostly dominated by the emittance pressure.

The matching section (a quadrupole quintuplet) is crucial for a proper beam matching to the BSM and the dogleg.

The doglegs are now parallel, but they lay on two different horizontal planes, 5.3 cm apart, as their respective IPs.

Fig. 17 – Laminarity parameter along the beamline, measuring the relative importance of space charge effects vs. emittance pressure.

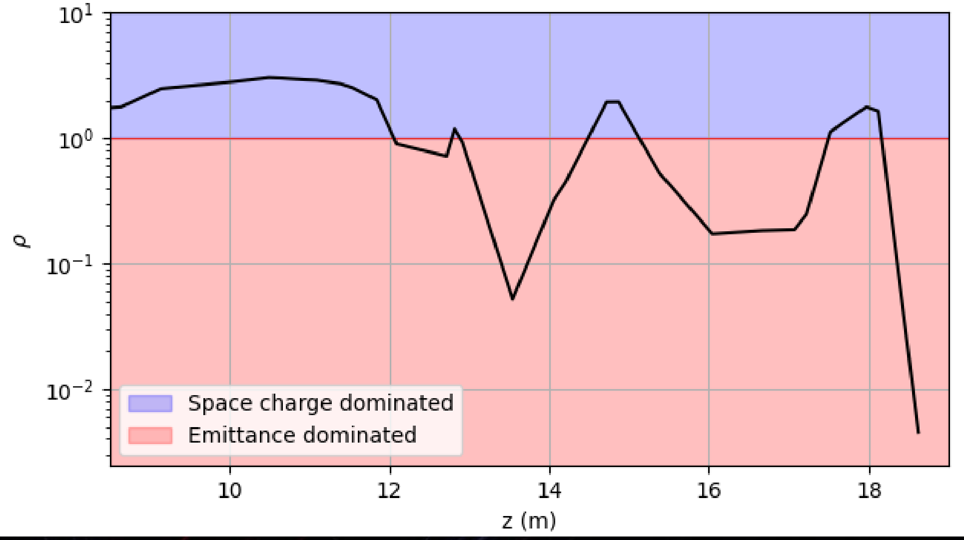

Beam transport and focusing to the IP

Fig. 18 – Beam dynamics simulation along the the beamline.

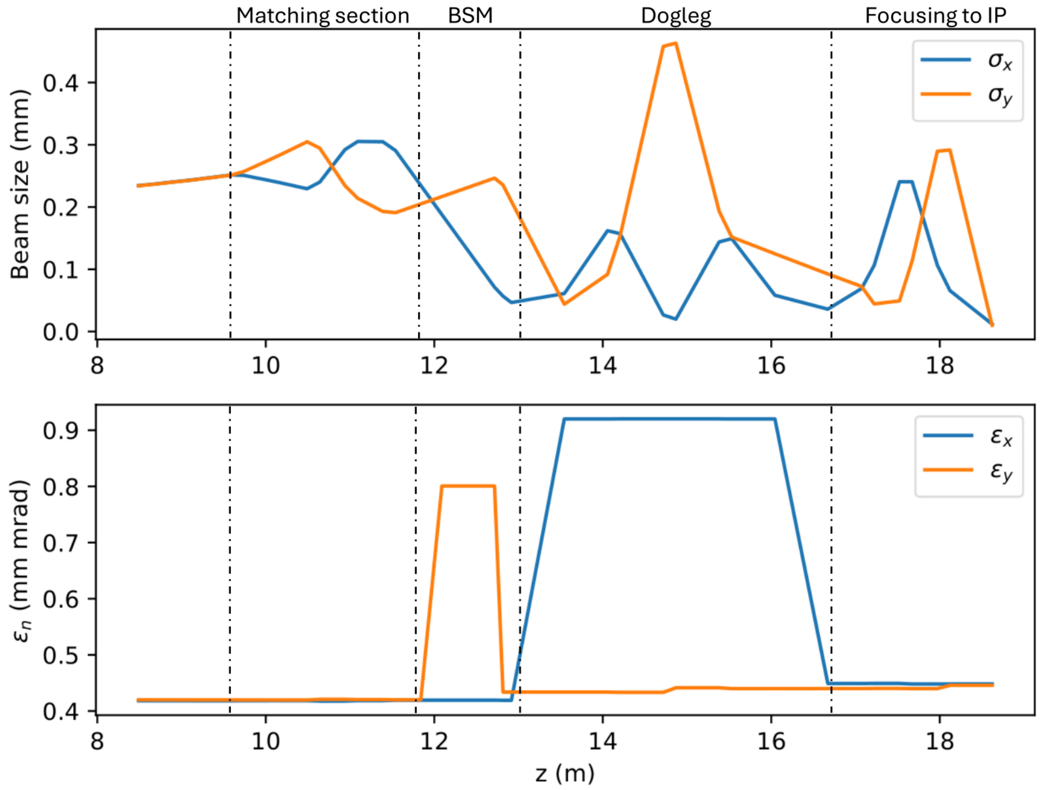

Fig. 19 – Dispersion functions along the beamline.

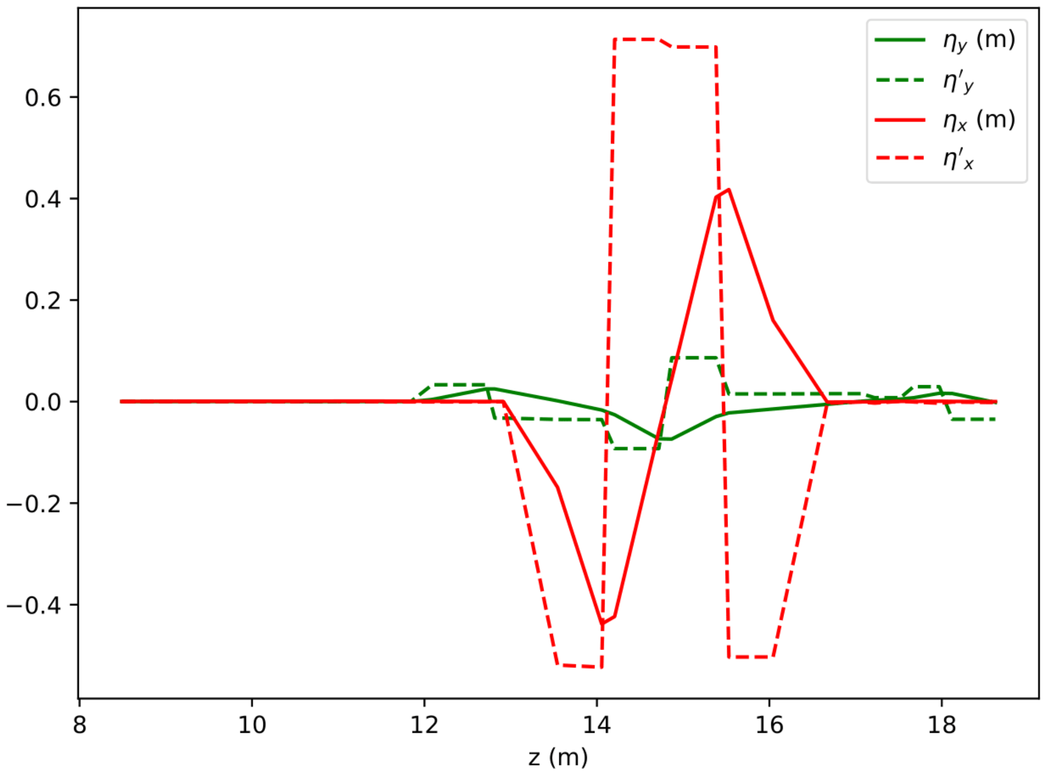

Beam transport and focusing to the IP

Fig. 18 – Beam dynamics simulation along the the beamline.

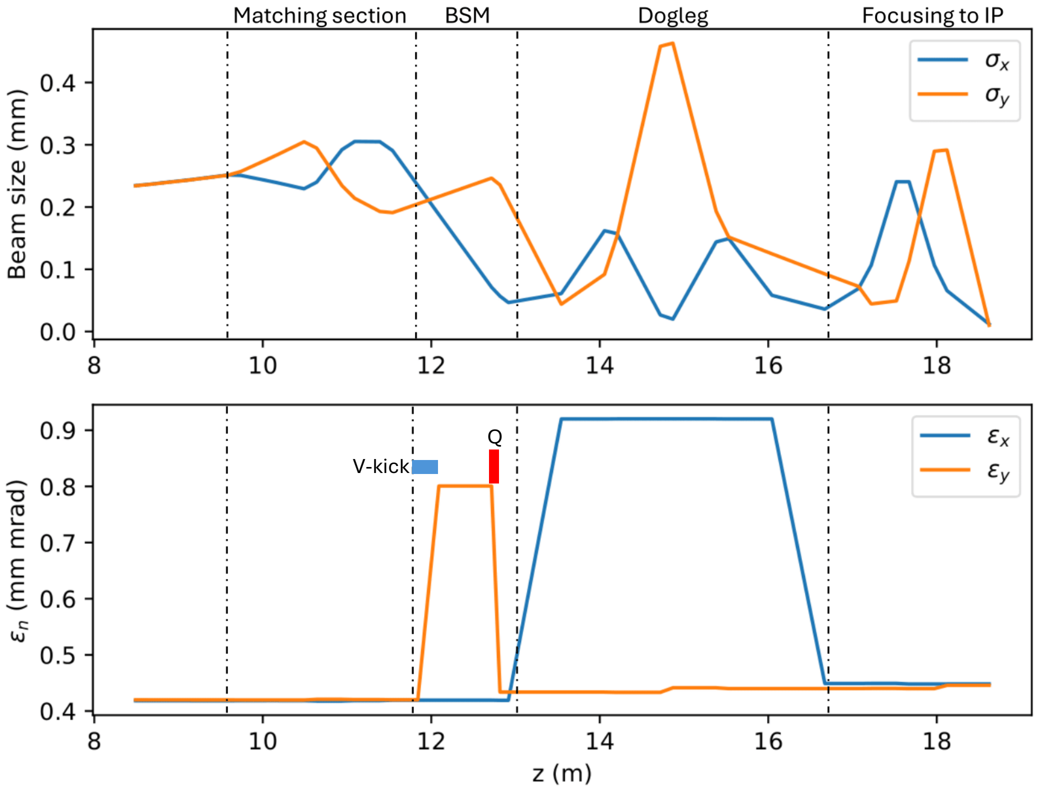

Fig. 19 – Dispersion functions along the beamline.

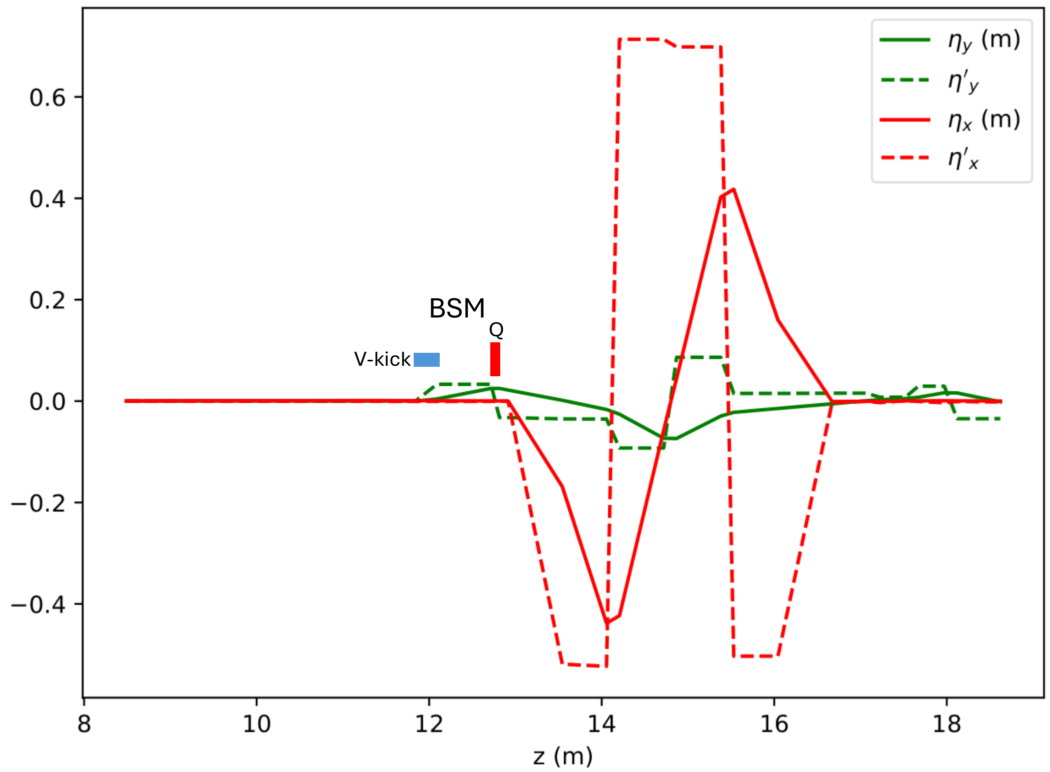

The BSM deflects the beam, acting as a vertical micro-dogleg and introducing a small vertical dispersion that cannot be corrected.

Beam transport and focusing to the IP

Fig. 18 – Beam dynamics simulation along the the beamline.

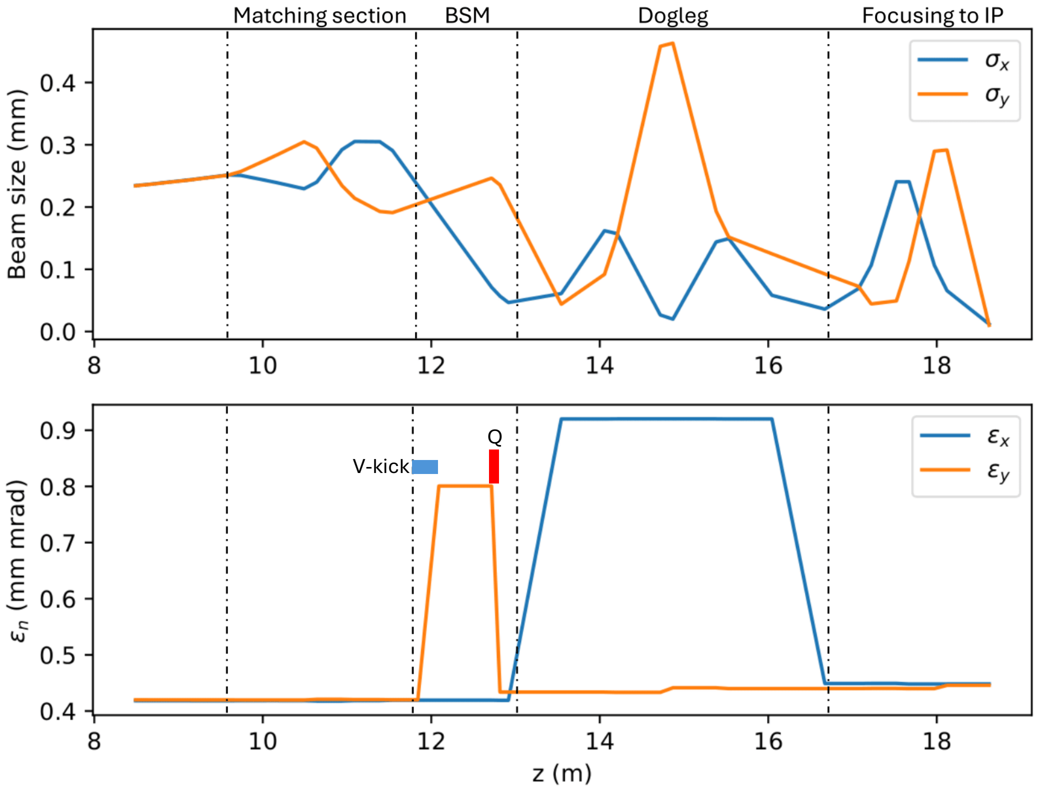

Fig. 19 – Dispersion functions along the beamline.

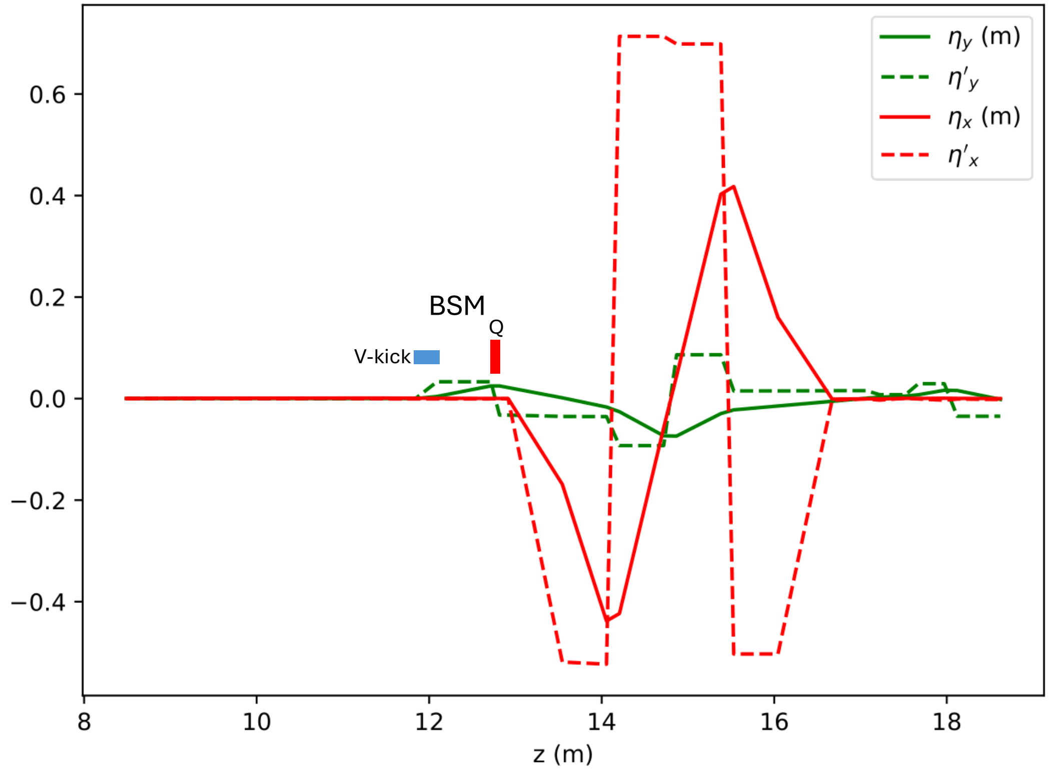

The BSM deflects the beam, acting as a vertical micro-dogleg and introducing a small vertical dispersion that cannot be corrected.

The double action of the BSM off-axis quadrupole (bending + focusing), combined with a fine tuning of the matching section, provides the proper coupling of the betatron motion to the chromatic motion in order to minimise the dispersion contribution to the vertical projected emittance.

Dispersion contribution to the projected emittance

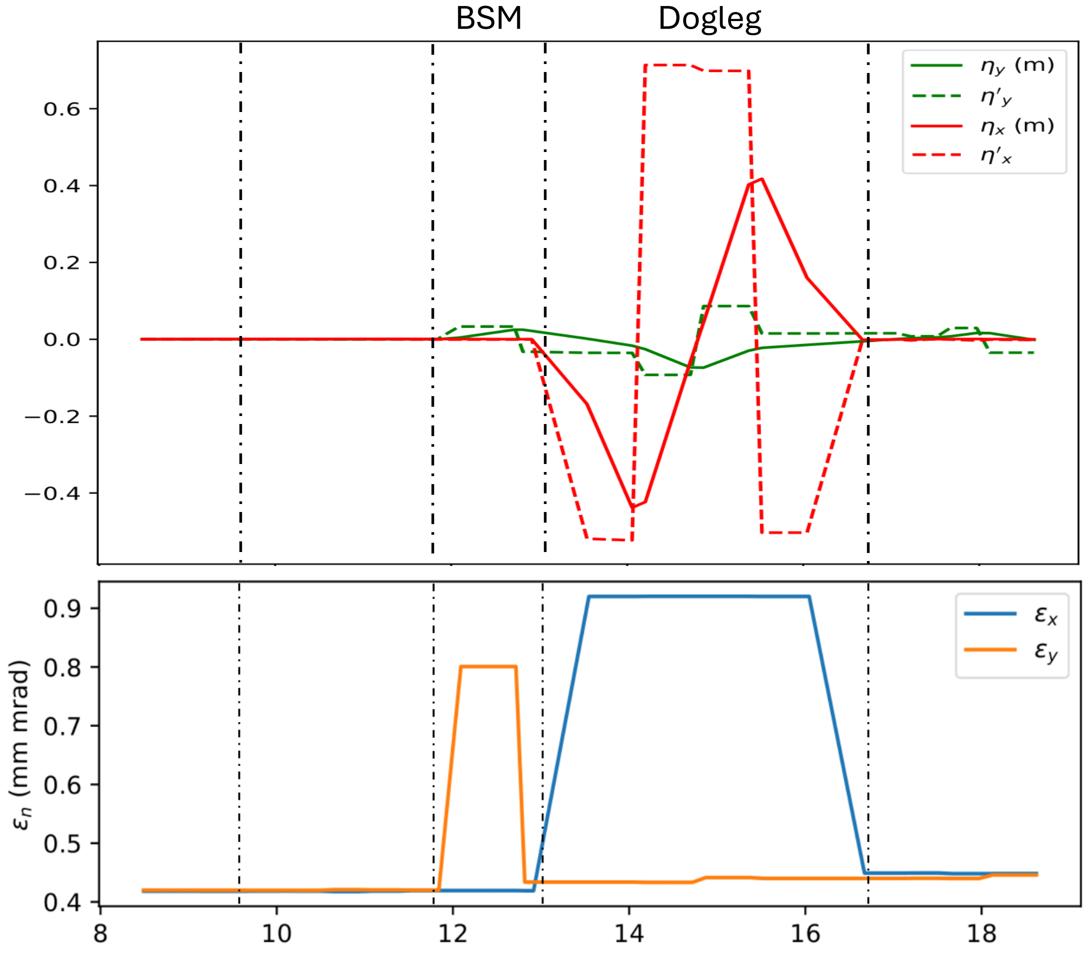

Fig. 20 – Dispersion functions (top) and beam projected emittance (bottom) along the beamline.

Chromatic $\mathcal{H}$-function

$$\gamma\eta^2 + 2\alpha\eta\eta' + \beta\eta'^2 = \mathcal{H}$$

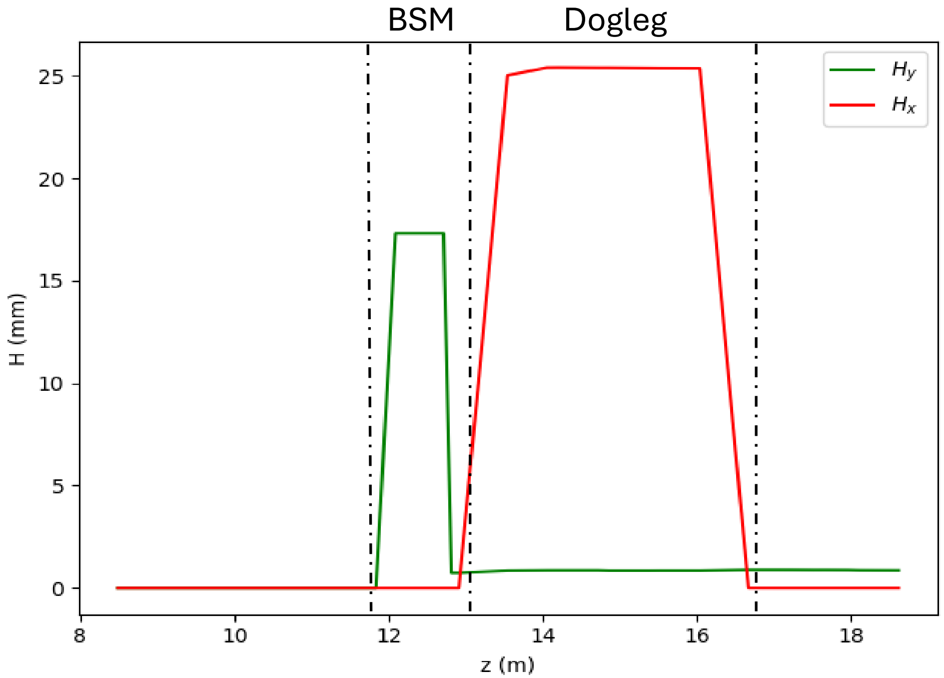

Fig. 21 – $\mathcal{H}$-functions along the beamline.

Beam parameters at the IP

Tab. 6 – Electron beam parameters at IP

Parameter	Value
Bunch charge [nC]	0.5
Beam energy [MeV]	145
Norm. proj. emittance [mm mrad]	0.45
Bunch length, rms [ps]	2.2
Horizontal beam size, rms [μm]	12.0
Vertical beam size, rms [μm]	10.0
Relative energy spread, rms [%]	0.03
Peak current [A]	71

Fig. 22 – Slice analysis of the electron beam at IP.

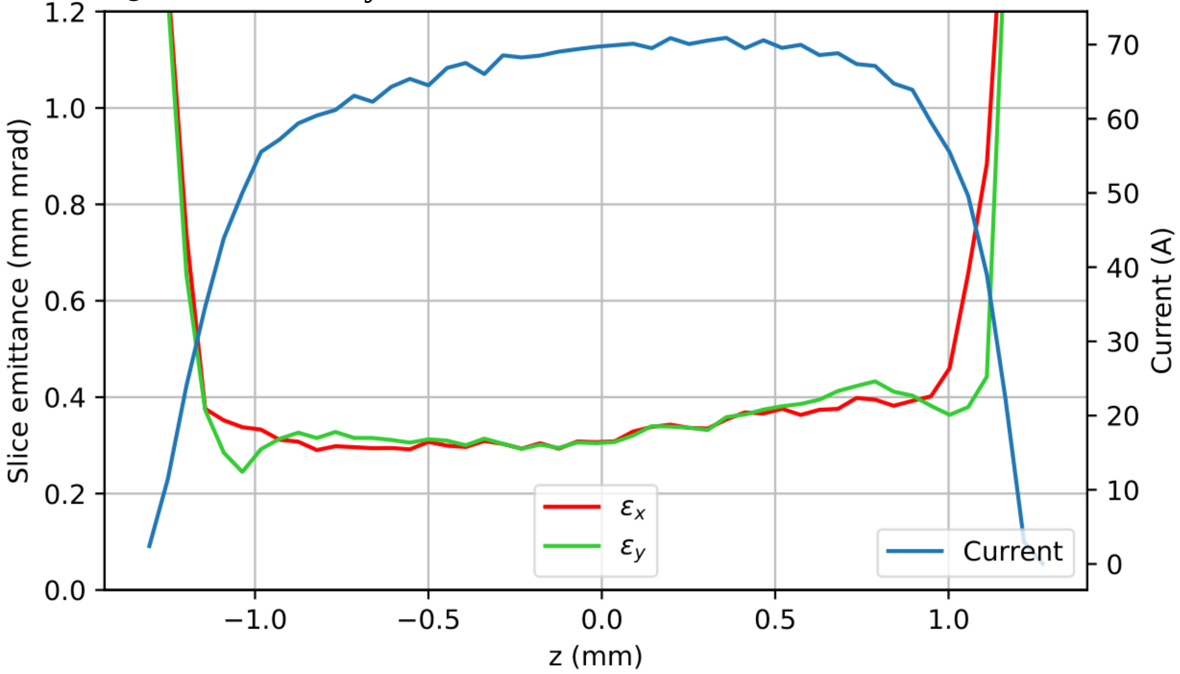

Laser and Optical box

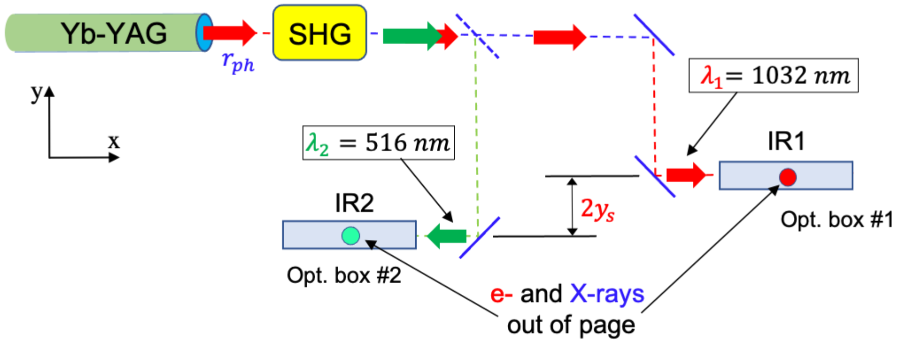

Fig. 23 – Dual-frequency operation in the Multimode BoCXS scheme adopting Second Harmonic Generation (SHG). The optical boxes are vertically separated by the $2y_s$=5.3 cm offset.

Tab. 7 – Laser parameters at IP

Parameter	Value
Rep. rate [kHz]	0.1
Central wavelength [nm]	1032-516
Bandwidth, FWHM [%]	1
Beam quality factor	<1.5
Pulse energy [J]	1.0
Intensity pulse size, rms [μm]	10.0
Pulse duration, rms [ps]	3.0

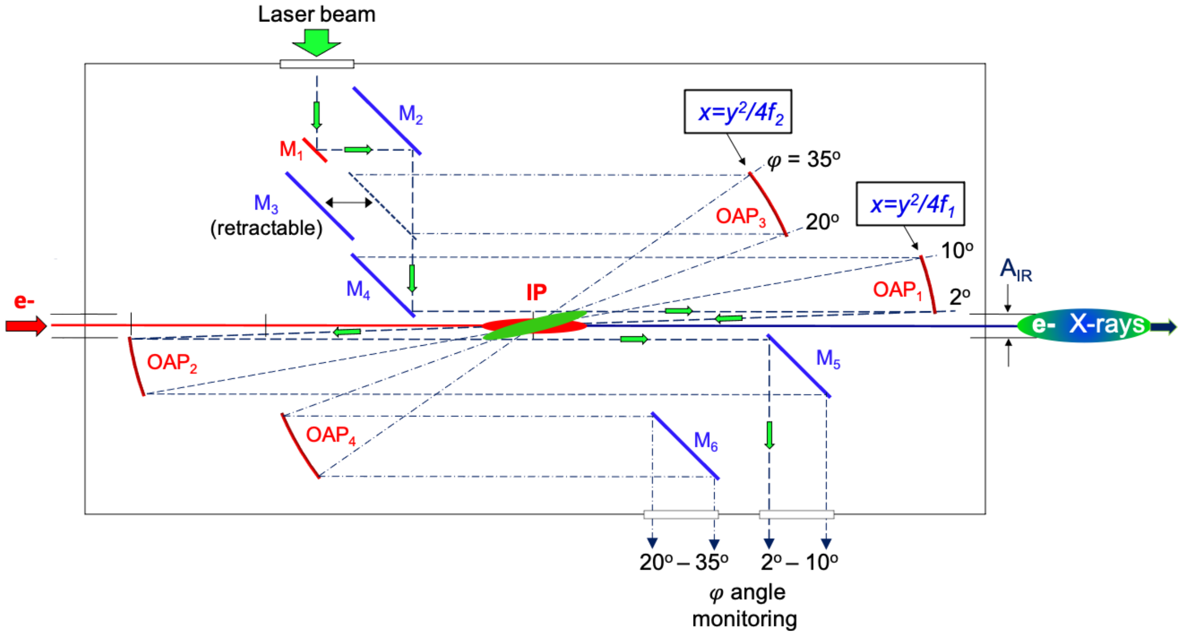

Fig. 24 – Layout of the optical box at one of the BoCXS laser-electron interaction regions. Two sets of OAP mirrors select the interaction angle φ within an operational range $\Delta\varphi_1 = 2^o - 10^o$ (M_4 – OAP_1) and a larger set $\Delta\varphi_2 = 20^o - 35^o$ (M_3 – OAP_3) to produce X-ray energy shifts of the order of 2–3 keV for KES dual-energy imaging. The angle φ is defined by the position of the scanning mirror M_1 and monitored through the $M_{5,6}$ extracting mirrors.

X-rays expected parameters

Tab. 8 – Compton X-ray expected parameters for an interaction angle of 2 deg

Parameter	1° laser harmonic	2° laser harmonic
Rep. rate [kHz]	0.1	
Pulse duration, rms [ps]	2.7	
Source size, rms [μm]	5.1	
Source divergence, rms [mrad]	2.7	
Max. photon energy [keV]	384.5	769.0
Relative bandwidth, FWHM [%]	29.3	
Total peak intensity [ph/pulse]	$3.7 \cdot 10^{8}$	$1.9 \cdot 10^{8}$
Total peak power [W]	$2.8 \cdot 10^{6}$	
Total average intensity [ph/s]	$3.7 \cdot 10^{10}$	$1.9 \cdot 10^{10}$
Total average power [W]	$7.6 \cdot 10^{-4}$	
Peak brilliance [ph/s/mm²/mrad²/0.1%BW]	$1.0 \cdot 10^{19}$	$5.0 \cdot 10^{18}$
Average brilliance [ph/s/mm²/mrad²/0.1%BW]	$6.8 \cdot 10^{9}$	$3.4 \cdot 10^{9}$
Average spectral density [ph/s/0.1%BW]	$5.6 \cdot 10^{7}$	$2.8 \cdot 10^{7}$

Fig. 25 – ICS intensity vs. photon energy (blue) and average photon energy vs. observation angle (red).

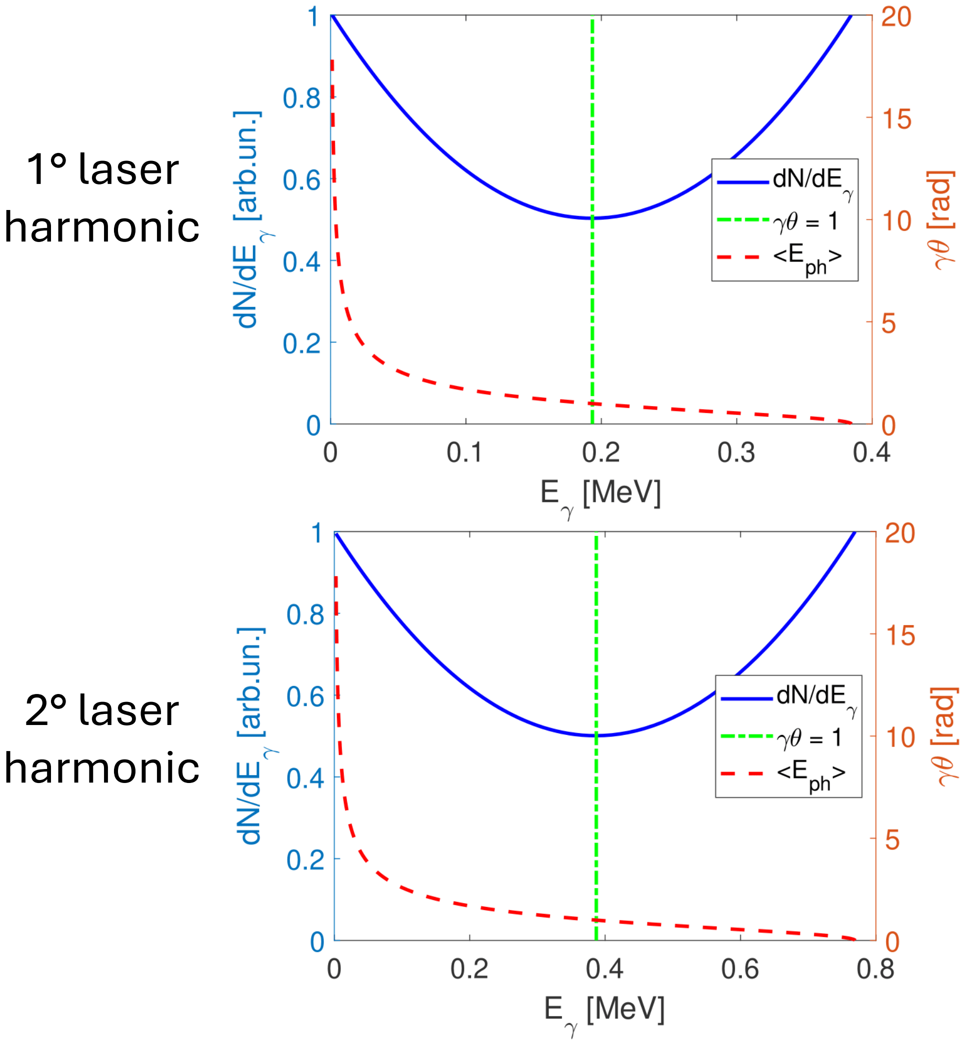

Future developments

SIMULATIONS

Simulation with space charge effects (start to end).

Stability studies (errors, jitters…).

Simulation of inverse Compton scattering.

Characterisation of the X-ray beam for specific applications.

BoCXS

Bologna Compton X-ray Source

Thank you for your attention